A Finite-Strain Phase-Field Description of Thermomechanically-Induced Fracture in Shape Memory Alloys

M.M. Hasan \cdot M. Zhang \cdot T. Baxevanis

Abstract A finite-strain, phase-field model for thermomechanically-induced fracture in shape memory alloys (SMAs), i.e., fracture under loading paths that may take advantage of either the superelastic response or the shape memory effect in SMAs, is presented based on the Eulerian logarithmic (Hencky) strain and the logarithmic objective rate. Based on experimental observations suggesting that SMAs fracture in a stress-controlled manner, damage is assumed to be driven by the elastic energy, i.e., phase transformation is assumed to contribute in crack formation and growth indirectly through stress redistribution. The model is restricted to quasistatic mechanical loading (no latent heat effects) and thermal loading sufficiently slow with respect to the time rate of heat transfer by conduction (no thermal gradients), and can describe phase transformation and orientation of martensite variants from a self-accommodated state. A single fracture toughness value is assumed, that of martensite, thus, the temperature range of interest is below M_d , which is the temperature above which the austenite phase is stable. The numerical implementation of the model in an efficient scheme is described and its ability to reproduce experimental observations on the fracture response of SMAs and handle complex geometries and loading conditions is demonstrated.

1 Introduction

Shape memory alloys (SMAs) undergo large, hysteretic, stress–strain–temperature excursions when subjected to appropriate thermomechanical loading due to a reversible, solid to solid, phase transformation from austenite to martensite [1–6]. Toughness enhancement during crack advance, *i.e.*, slow and stable crack extension, is observed in these materials associated with *extrinsic* shielding resulting from inelastic deformation left in the wake of the advancing crack [7–10], similarly to ductile materials. Transformation from austenite to martensite [11–21], and *vice versa* [11, 22, 23], (re)orientation of martensite variants [23, 24], transformation-induced contraction [25], overload and transformation-induced plasticity [20, 24, 26, 27], and thermomechanical coupling associated to latent heat [28, 29] have an impact on the toughness enhancement observed. Large-scale phase transformation in front of a crack, resulted, for example, due to thermal actuation, promotes crack advance, counteracting the aforementioned stabilizing effect of the irrecoverable deformation left in the crack's wake [27, 30–32].

Despite the aforementioned apparent similarity with the fracture response of ductile materials, SMAs belong to a relatively brittle class of materials, that of intermetallics, and fail by cleavage of crystallo-

M.M. Hasan

Department of Mechanical Engineering, University of Houston, TX 77204-4006. E-mail: mshaibal48@gmail.com

M. Zhang

 $Department \ of \ Mechanical \ Engineering, \ University \ of \ Houston, \ TX \ 77204-4006. \ E-mail: \ mengqian.zhang 1991@gmail.com$

Γ. Baxevanis

Department of Mechanical Engineering, University of Houston, TX 77204-4006. E-mail: tbaxevanis@uh.edu

graphic planes, which, depending on the local precipitate size and concentration, is assisted by ductile tearing [8, 33–35]. Experimental observations [34] and unit cell studies [36] suggest that the work expended on the *intrinsic* damage mechanisms, *i.e.*, void nucleation and growth, has a minor contribution to the work balance during crack growth, which is stress-driven. Currently, the numerical investigations of fracture of SMAs either totally ignore the fracture process or, as customary for elastic–plastic materials, couple a fracture process model to the deformation field of a growing crack. The former investigations, which are further justified by direct evidence of restricted dislocation activity close to the crack tip as compared to conventional ductile materials [37], are either based on (i) linear elastic fracture mechanics tools, assuming that the mechanical fields in the near-tip region are dictated by a linear elastic response, such as the virtual crack closure technique [26, 30], or (ii) nonlinear elastic fracture mechanics tools to simulate steady-state crack growth based on the path-independence of the *J*-integral in such conditions [12, 13, 22, 23, 28]. The latter investigations model the fracture process with cohesive elements obeying a bilinear traction–separation law described by the cohesive strength σ_c and the work of separation *G* along the crack plane [11, 16]. The calibration of the phenomenological traction–separation parameters, chosen to give best fit of crack growth experimental data, is a formidable task in SMAs.

The aim, herein, is to develop a phenomenological continuum model for SMAs within the framework of the phase-field approach to fracture. The major advantage of the phase-field approach over the aforementioned discrete fracture models lies on its ability to model crack nucleation, complex crack patterns, branching and merging, in both 2D and 3D, without ad hoc additions to the theory and without adaptive mesh refinement for sufficiently fine mesh resolutions. This stems from the regularization of the sharp crack surface topology by a diffusive crack zone governed by a scalar auxiliary variable, a phase field, which interpolates between the unbroken and the broken state of the material. In the phase-field approach to fracture, also known as variational approach to fracture [38, 39], the solution to the fracture problem is found as the minimizer of a global energy functional that includes a volumetric approximation of total fracture energy. Thus far, the phase-field approach to fracture has been focused mostly on brittle materials [40–57] with proposed modifications to fracture in ductile materials [58–67], composites [68–70], rubbery polymers [71–73], hydrogen embrittlement [74, 75], hydraulic fracturing [76–79], geomaterials [80–86] and piezoelectric solids [87]. Recently, the phase-field approach to fracture has been extended to fatigue as well [88–104].

The proposed model accounts for reversible phase transformation from austenite to self-accommodated and/or oriented martensite, orientation of martensite variants, temperature and load dependence of the hysteresis width, asymmetry between forward and reverse phase transformation, and is flexible enough to address the deformation response in the concurrent presence of several phases, i.e., when austenite, self-accommodated and oriented martensite co-exist in the microstructure. The model is formulated based on the Eulerian logarithmic strain, sometimes referred to as true or natural or Hencky strain, which is the only strain measure that its corotational rate (associated with the so-called logarithmic spin) is the rate of deformation tensor, also-called stretching [105, 106]. Additive split of the rate of deformation results in an additive decomposition of strain and, thus, in a simple model structure and an easy implementation procedure. The model adopts a single value for the energy expended to create new surfaces, which corresponds to the fracture toughness of martensite. Thus, the model is applicable for temperatures below M_d , since, as recently shown [36, 107], the fracture toughness of SMAs is piece-wise constant with respect to temperature, below and above M_d , with the value below M_d corresponding to the fracture toughness of martensite and that above corresponding to austenite. For nominal temperatures above M_d the austenite phase is stable and the deformation response of the SMA is similar to that of a conventional metal. Furthermore, the model neglects plastic deformation and assumes that inelastic deformation associated with phase transformation and orientation of martensite variants contributes to the fracture response only through stress redistribution, underpinning the experimental evidence [108] and numerical studies [108, 109] that the fracture process in SMA is stress-driven. The model is shown to reproduce experimental observations, such as fracture during cooling under a constant bias load, transformation and/or orientation-induced toughening, and it is verified on complex geometries and loading conditions, including mixed-mode fracture.

It should be noted that recently a phase-field model for fracture of SMAs was proposed in literature [110, 111], which in contrast to the one proposed herein (i) is formulated under the small-strain assumption, (ii) is restricted to phase transformation, *i.e.*, cannot describe orientation of self-accommodated martensite, (iii) is restricted to isothermal mechanical loading conditions, and (iv) assumes that fracture is driven by the total strain energy density, *i.e.*, assumes that the total work of transformation-induced deformation can be directly expended on the intrinsic damage mechanisms.

The remaining of the paper is organized as follows. In Section 2, the model's formulation by postulating a microforce balance is described. In Section 3, verification simulations are presented depicting the model's ability to capture the experimentally observed fracture response of SMAs under mechanical and/or actuation loading. A summary of the paper is given in Section 4.

2 Formulation

2.1 Kinematics

Let Q_0 define the reference configuration of a continuum body, with its particles associated with their position $\mathbf{X} \in Q_0$, undergoing a motion $\varphi_t : Q_0 \to Q_t$, where $t \in \mathbf{R}$ is the time, Q_t is the current configuration, and the particles' current position is labeled $\mathbf{x} \in Q_t$.

The Eulerian logarithmic strain

$$\mathbf{h} = \frac{1}{2} \ln \mathbf{b} = \sum_{\alpha=1}^{m} \ln \lambda^{\alpha} \mathbf{b}^{\alpha}, \tag{2.1}$$

is defined as the logarithmic measure of the left Cauchy-Green deformation tensor $\mathbf{b} = \mathbf{F}\mathbf{F}^T$ ($\mathbf{F} = \partial_{\mathbf{X}}\varphi_t$ is the deformation gradient, λ^{α} are the m distinct eigenvalues of \mathbf{b} , \mathbf{b}^{α} are the corresponding eigenprojections, and the notation $\partial_{\mathbf{a}}$ denotes differentiation with respect to the generic variable \mathbf{a}) and its conjugate Kirchhoff stress

$$\tau = J\sigma, \tag{2.2}$$

where $J = \det \mathbf{F} > 0$ is the Jacobian of the deformation and $\boldsymbol{\sigma}$ the Cauchy stress.

The Eulerian logarithmic (Hencky) strain is the only strain measure whose objective time rate with respect to a corrotational frame yields the total stretching (or rate of deformation) $\mathbf{D} = \frac{1}{2} \left(\mathbf{L} + \mathbf{L}^T \right)$, where $\mathbf{L} = \dot{\mathbf{F}}\mathbf{F}^{-1}$ stands for the velocity gradient, *i.e.*,

$$\dot{\mathbf{h}} = \dot{\mathbf{h}} + \mathbf{h}\Omega^L - \Omega^L \mathbf{h} = \mathbf{D},\tag{2.3}$$

where the superscript " \degree " denotes the objective logarithmic time rate of any tensor a

$$\mathring{\boldsymbol{a}} = \dot{\boldsymbol{a}} + \boldsymbol{a} \boldsymbol{\Omega}^L - \boldsymbol{\Omega}^L \boldsymbol{a}, \tag{2.4}$$

defined by the logarithmic spin $\mathbf{\Omega}^L = \mathbf{W} + \sum_{\alpha \neq \beta}^n \left(\frac{1 + (\lambda^{\alpha}/\lambda^{\beta})}{1 - (\lambda^{\alpha}/\lambda^{\beta})} + \frac{2}{\ln(\lambda^{\alpha}/\lambda^{\beta})} \right) \mathbf{b}^{\alpha} \mathbf{D} \mathbf{b}^{\beta}$ ($\mathbf{W} = \frac{1}{2} \left(\mathbf{L} - \mathbf{L}^T \right)$ is the vorticity and "·" denotes material time rate.)

On account of (2.4), relation

$$\overline{\mathbf{R}^L a \mathbf{R}^{L^T}} = \mathbf{R}^L \mathring{a} \mathbf{R}^{L^T} \tag{2.5}$$

holds, where the logarithmic rotation, \mathbf{R}^{L} , is defined from the differential equation

$$\dot{\mathbf{R}}^L = \mathbf{\Omega}^L \mathbf{R}^L; \quad \mathbf{R}^L|_{t=0} = \boldsymbol{\delta}, \tag{2.6}$$

where δ is the unit tensor with components $\delta_{ij} = 1$ if i = j and $\delta_{ij} = 0$ if $i \neq j$. The left hand side of (2.5) represents the material time rate of a Lagrangian quantity and, thus, (2.6) generates a one-parameter subgroup of rotations that define a locally rotating coordinate system in which the material time rates

of the obtained rotated tensors remain unaltered by superposed spatial rigid body motions [106]. Time integration of (2.5), assuming a = h and $h|_{t=0} = 0$, yields

$$\mathbf{h} = \mathbf{R}^{LT} \left(\int_0^t \mathbf{R}^L \mathring{\mathbf{h}} \mathbf{R}^{LT} dt \right) \mathbf{R}^L \stackrel{\text{(2.3)}}{=} \mathbf{R}^{LT} \left(\int_0^t \mathbf{R}^L \mathbf{D} \mathbf{R}^{LT} dt \right) \mathbf{R}^L, \tag{2.7}$$

and, thus, additive decomposition of total stretching \mathbf{D} results in additive decomposition of the Hencky strain.

2.2 Conservation Principles

The phase-field model for fracture of SMAs is derived by postulating a microforce balance [112]. The local forms of the postulated balance laws are derived from their respective global forms, given below, which hold for all subgerions \mathcal{B}_t of the continuum body, \mathcal{Q}_t , with a sufficiently smooth boundary $\partial \mathcal{B}_t$. All integrands are at least C^0 -continuous.

2.2.1 Balance of mass

$$\int_{\mathcal{B}_0} \rho_0 \, d\mathbf{X} = \int_{\mathcal{B}_+} \rho \, d\mathbf{x} \Rightarrow \rho_0 = \rho J,\tag{2.8}$$

where ρ (ρ_0) is the mass density per unit (reference) volume.

2.2.2 Balance of linear momentum (equilibrium)

$$\int_{\partial \mathcal{B}_t} \mathbf{t} \, ds + \int_{\mathcal{B}_t} \rho \mathbf{b} \, d\mathbf{x} = 0 \Rightarrow \nabla_{\mathbf{x}} \cdot \boldsymbol{\tau} + \rho_0 \mathbf{b} = 0, \tag{2.9}$$

where $\mathbf{t} = \boldsymbol{\sigma} \cdot \mathbf{n}$ denotes the traction, \mathbf{b} the body force, \mathbf{n} the outward unit normal of $\partial \mathcal{B}_t$, and $\nabla_{\boldsymbol{x}}$ the divergence operator.

2.2.3 Balance of angular momentum

$$\int_{\partial \mathcal{B}_t} \mathbf{r} \times \mathbf{t} \, ds + \int_{\mathcal{B}_t} \mathbf{r} \times \rho \mathbf{b} \, d\mathbf{x} = 0 \Rightarrow \mathbf{\tau} = \mathbf{\tau}^T, \tag{2.10}$$

where \mathbf{r} denotes the position vector of a material point and \times is the cross product between two vectors.

2.2.4 Microforce balance

An internal scalar microforce π and a vector stress $\boldsymbol{\zeta}$ that exerts a scalar traction $\boldsymbol{\zeta} \cdot \mathbf{n}$ on $\partial \mathcal{B}_t$ are postulated [112],

$$\int_{\partial \mathcal{B}_t} \boldsymbol{\zeta} \cdot \mathbf{n} \, ds + \int_{\mathcal{B}_t} \rho \pi \, d\boldsymbol{x} = 0 \Rightarrow \boldsymbol{\nabla}_{\boldsymbol{x}} \cdot \boldsymbol{\zeta} + \rho \pi = 0. \tag{2.11}$$

2.2.5 Energy balance

The energy balance is stated as

$$\overline{\int_{\mathcal{B}_{t}} \rho u \, d\mathbf{x}} = \int_{\partial \mathcal{B}_{t}} \mathbf{t} \cdot \dot{\mathbf{u}} \, ds + \int_{\mathcal{B}_{t}} \rho \mathbf{b} \cdot \dot{\mathbf{u}} \, d\mathbf{x} + \int_{\partial \mathcal{B}_{t}} (\boldsymbol{\zeta} \cdot \mathbf{n}) \dot{c} \, ds + \int_{\mathcal{B}_{t}} \rho r \, d\mathbf{x} - \int_{\partial \mathcal{B}_{t}} \mathbf{q} \cdot \mathbf{n} \, ds$$

$$\stackrel{(\mathbf{2.11})}{\Rightarrow} \rho \dot{u} = \frac{1}{J} \boldsymbol{\tau} : \mathring{\mathbf{h}} + \boldsymbol{\zeta} \cdot \partial_{\mathbf{x}} \dot{c} - \rho \pi \dot{c} + \rho r - \boldsymbol{\nabla}_{\mathbf{x}} \cdot \mathbf{q}, \quad (2.12)$$

where u is the internal energy per unit mass density, u is the displacement vector, c is the phase-field parameter (or order parameter) to be further defined below, \mathbf{q} is the heat flux, and r is a heat source.

Under the assumptions r=0 and $\nabla_x \cdot \mathbf{q}=\mathbf{0}$, the above equation simplifies to

$$\rho \dot{u} = \frac{1}{J} \boldsymbol{\tau} : \mathring{\mathbf{h}} + \boldsymbol{\zeta} \cdot \partial_{\boldsymbol{x}} \dot{c} - \rho \pi \dot{c}. \tag{2.13}$$

2.2.6 Entropy inequality principle

Under the above assumptions, the second law of thermodynamics reads as

$$\frac{\dot{}}{\int_{\mathcal{B}_t} \rho s dx} \ge -\int_{\partial \mathcal{B}_t} \frac{\mathbf{q} \cdot \mathbf{n}}{T} \, ds \Rightarrow \rho \dot{s} \ge \frac{\mathbf{q} \cdot \partial_x T}{T^2},$$

where s is the entropy per unit mass density and T is the absolute temperature.

Assuming $\partial_x T = \mathbf{0}$, the entropy inequality principle can be stated in terms of dissipation, D, as

$$D = \rho \dot{s}T \ge 0,\tag{2.14}$$

In view of the energy balance equation (2.13) and the Legendre transformation,

$$u = G + \frac{1}{\rho_0} \boldsymbol{\tau} : \mathbf{h} + Ts, \tag{2.15}$$

where G is the Gibbs free energy, the dissipation inequality can be further stated as

$$D = -\frac{1}{I}\mathring{\boldsymbol{\tau}} : \mathbf{h} - \rho s \dot{T} + \boldsymbol{\zeta} \cdot \partial_{\boldsymbol{x}} \dot{c} - \rho \pi \dot{c} - \rho \dot{G} \ge 0.$$
 (2.16)

The assumption of a uniform throughout the material, at every instant, temperature distribution, $\partial_x T = \mathbf{0}$, corresponds to assuming the rate of both the mechanical and thermal loading being sufficiently slow with respect to the time rate of heat transfer by conduction.

2.3 Constitutive Response

The constitutive equations can be derived in a thermodynamically consistent manner by postulating the Gibbs free energy and a volumetric approximation of total fracture energy.

The total strain tensor, h, is decomposed

$$\mathbf{h} = \mathbf{h}^e + \mathbf{h}^{in} = \mathbf{h}^e + \mathbf{h}^t + \mathbf{h}^o, \tag{2.17}$$

into a elastic, \mathbf{h}^e , and inelastic, \mathbf{h}^{in} , part. The inelastic part is further decomposed into \mathbf{h}^t and \mathbf{h}^o , representing the strain contributions of transformation from austenite to martensite and orientation of self-accommodated martensite, respectively¹.

Note that thermal strains are neglected, an approximation that restricts the model to temperature ranges required for the shape memory effect within which thermal strain is an order of magnitude smaller

 $^{^{1}}$ Oriented martensite forms from self-accommodated martensite under mechanical load with or without thermal inputs.

than the transformation strain. The thermal expansion of oriented martensite is anisotropic, dependent on the volume fraction of oriented martensite and the orientation direction, and its implementation is described in [123].

The logarithmic rate of the inelastic strain tensor is taken to be

$$\mathring{\mathbf{h}}^{in} = \mathring{\mathbf{h}}^{o} + \mathring{\mathbf{h}}^{t} = \sqrt{\frac{3}{2}} \left(\xi \dot{H} \mathbf{N}^{o} + \dot{\xi} H \mathbf{N}^{t} \right), \tag{2.18}$$

where the martensite volume fraction, ξ , is restricted by $0 \le \xi \le 1$ and the effective inelastic strain, H, by $0 \le H \le H^{\max}$, \mathbf{N}^o and \mathbf{N}^t are the flow directions for orientation and phase transformation, respectively. The multiplier $\sqrt{3/2}$ has been introduced so that H is the measure of the effective inelastic strain, *i.e.*, $H = \sqrt{\frac{2}{3}\mathbf{h}^{in} : \mathbf{h}^{in}}$. It is noted that ξH can be interpreted as $\xi^o H^{\max}$, where $\xi^o = \xi H/H^{\max}$ denotes the oriented martensite volume fraction.

The volumetric approximation of total fracture energy adopted is through a crack density functional Γ_c

$$\int_{\Gamma_t} G_c ds \approx \int_{\mathcal{Q}_t} \mathcal{G}_c \Gamma_c(c, \partial_{\boldsymbol{x}} c) d\boldsymbol{x}, \tag{2.19}$$

where the evolving internal discontinuity boundary, Γ_t , represents a set of discrete cracks, \mathcal{G}_c is the energy expended to create a unit area of fracture surface, and the damage-like, phase-field variable, $0 \le c \le 1$, approximates the fracture surfaces, taking the value 0 away from the crack and the value 1 within the crack. The crack density functional is typically given as

$$\Gamma_c(c, \partial_{\boldsymbol{x}}c) = \frac{1}{4\ell} \left(c^2 + 4\ell^2 \partial_{\boldsymbol{x}}c \cdot \partial_{\boldsymbol{x}}c \right), \tag{2.20}$$

where $\ell > 0$ is a model length parameter that controls the width of the smooth approximation of the cracks.

2.3.1 Thermodynamic Potential

The Gibbs free energy potential, G, is defined as

$$G(\boldsymbol{\tau}, T, \boldsymbol{\xi}, \mathbf{h}^{in}, \kappa^{o}, \kappa^{t}, \kappa^{r}, c, \partial_{\boldsymbol{x}} c) = G^{d}(\boldsymbol{\tau}, T, \boldsymbol{\xi}, \mathbf{h}^{in}, \kappa^{o}, \kappa^{t}, \kappa^{r}, c) + \mathcal{G}_{c} \Gamma_{c}(c, \partial_{\boldsymbol{x}} c) \stackrel{\text{(2.20)}}{=}$$

$$- \frac{1}{\rho_{0}} m^{-1}(c) W_{\boldsymbol{\tau}} + c(\boldsymbol{\xi}) \left[T - T_{0} - T \ln \left(\frac{T}{T_{0}} \right) \right] - s_{0}(\boldsymbol{\xi}) T + u_{0}(\boldsymbol{\xi}) - \frac{1}{\rho_{0}} \boldsymbol{\tau} : \mathbf{h}^{in}$$

$$+ \frac{1}{\rho} g^{o}(\kappa^{o}) + \frac{1}{\rho} g^{t}(\kappa^{t}) + \frac{1}{\rho} \frac{\mathcal{G}_{c}}{4\ell} \left[c^{2} + 4\ell^{2} \partial_{\boldsymbol{x}} c \cdot \partial_{\boldsymbol{x}} c \right], \quad (2.21)$$

where $W_{\tau} = \frac{1}{2}\tau : \mathbf{S}(\xi) : \tau$. The degradation function $0 \le m(c) \le 1$, is such that m(0) = 1, m(1) = 0, and m' < 0, where the prime denotes differentiation with respect to argument. The function $m(c) = (1-c)^2$ is assumed. The model parameters \mathbf{S} , \mathbf{c} , s_0 , and u_0 denote the compliance tensor, specific heat, specific entropy at the reference state, and specific internal energy at the reference state, respectively, which are assumed to be different for each phase, and the density ρ is assumed to be the same regardless of phase. The effective value of phase-dependent parameters, \mathbf{S} , \mathbf{c} , s_0 , and u_0 , in virtue of (2.21), are evaluated in terms of the martensite volume fraction, ξ , by the rule of mixtures, i.e., $\mathbf{a}(\xi) = \mathbf{a}^A + \xi \left(\mathbf{a}^M - \mathbf{a}^A\right) = \mathbf{a}^A + \xi \Delta \mathbf{a}$, where \mathbf{a} stands for any of the phase-dependent parameters. The internal state variables g^o and g^t describe the free energy blocked in the microstructure due to orientation and transformation, respectively, which depend only on the respective isotropic hardening variables, κ^t and κ^o .

2.3.2 Constitutive Relations

Inequality (2.16) reads, via chain rule differentiation on G with respect to the internal variables set, as

$$D = -\frac{1}{J}\mathring{\boldsymbol{\tau}} : \mathbf{h} - \rho s \dot{T} - \rho \partial_{\boldsymbol{\tau}} G : \mathring{\boldsymbol{\tau}} - \rho \partial_{T} G \dot{T} - \rho \partial_{\xi} G \dot{\xi} - \rho \partial_{\boldsymbol{h}^{in}} G : \mathring{\mathbf{h}}^{in}$$
$$- \rho \partial_{\kappa^{t}} G \dot{\kappa}^{t} - \rho \partial_{\kappa^{o}} G \dot{\kappa}^{o} - \rho \partial_{\partial_{\boldsymbol{x}^{c}}} G \cdot \partial_{\boldsymbol{x}} \dot{c} - \rho \partial_{c} G \dot{c} + \boldsymbol{\zeta} \cdot \partial_{\boldsymbol{x}} \dot{c} - \rho \pi \dot{c} \ge 0. \quad (2.22)$$

Standard thermodynamical arguments, applied to the dissipation inequality (2.22), yield the constitutive relationships

$$\mathbf{h} = -\rho \partial_{\tau} G = m^{-1}(c) \frac{\partial W_{\tau}}{\partial \tau} + \mathbf{h}^{in} \stackrel{\text{(2.17)}}{\Rightarrow} \tau = m(c) \mathbf{C} : \mathbf{h}^{e}, \text{ where } \mathbf{C} = \mathbf{S}^{-1}$$
 (2.23)

$$s = -\partial_T G = \operatorname{c} \ln \left(\frac{T}{T_0} \right) + s_0, \tag{2.24}$$

$$\zeta = \rho \partial_{\partial_{\boldsymbol{x}}} c G = 2\mathcal{G}_c \ell \partial_{\boldsymbol{x}} c \tag{2.25}$$

and the reduced dissipation expression

$$D = p\dot{\xi} + \tau : (\mathring{\mathbf{h}}^t + \mathring{\mathbf{h}}^o) + \mu^t \dot{\kappa}^t + \mu^o \dot{\kappa}^o - (\rho_0 \pi + \mu^c) \dot{c} \ge 0,$$
 (2.26)

where

$$p = -\rho_0 \partial_{\xi} G = \frac{1}{2} m^{-1}(c) \boldsymbol{\tau} : \Delta \mathbf{S} : \boldsymbol{\tau} - \rho_0 \Delta c \left[T - T_0 - T \ln \left(\frac{T}{T_0} \right) \right] + \rho_0 \Delta s_0 T - \Delta u_0, \tag{2.27}$$

$$\mu^a = -\rho_0 \partial_{\kappa^a} G, \tag{2.28}$$

$$\mu^c = -\rho_0 \partial_c G, \tag{2.29}$$

and a stands for any of the superscripts o, t or r.

Assuming the material to be strongly dissipative, inequality (2.26) is satisfied if

$$\begin{cases}
D^{o} = \boldsymbol{\tau} : \mathring{\mathbf{h}}^{o} + \mu^{o} \dot{\kappa}^{o} > 0; & \mathring{\mathbf{h}}^{o} \neq \mathbf{0}, \\
D^{t} = p \dot{\xi} + \boldsymbol{\tau} : \mathring{\mathbf{h}}^{t} + \mu^{t} \dot{\kappa}^{t} > 0; & \dot{\xi} \neq 0, \\
D^{c} = -(\rho_{0} \pi + \mu^{c}) \dot{c} > 0; & \dot{c} > 0,
\end{cases}$$
(2.30)

are enforced. It is assumed that these inequalities are obeyed at all times so that the dissipation inequality is concurrently satisfied.

In view of (2.29) and (2.21), the above dissipation inequality (2.30c) reads as

$$D^{c} = -\left(\rho_{0}\pi - \partial_{c} \left[m^{-1}(c)\right] W_{\tau} + \frac{\mathcal{G}_{c}}{2\ell}c\right) \dot{c} \geq 0$$

and can be satisfied by assuming

$$\rho_0 \pi = \partial_c \left[m^{-1}(c) \right] W_{\tau} - \frac{\mathcal{G}_c}{2\ell} c. \tag{2.31}$$

2.3.3 Evolution of Internal State Variables

Inequalities (2.30) are used to determine the kinetic relations for the internal state variables, *i.e.*, the flow rules, as follows [113].

Flow rules associated with orientation.— A potential function associated with orientation is postulated

$$Q^{o}(\tau, \mu^{o}) \equiv \xi(\bar{\tau} - \mu^{o} - Y^{o}), \quad (\xi \neq 0)$$
 (2.32)

where $\bar{\tau} = \sqrt{\frac{3}{2}\tau':\tau'}$ stands for the von Mises Kirchhoff stress $(\tau' = \tau - \frac{1}{3}\mathrm{tr}(\tau)\delta)$ is the deviatoric Kirchhoff stress tensor), and Y^o is a positive scalar. Assuming generalized normality, the orientation related internal state variables then read as

$$\begin{cases}
\mathring{\mathbf{h}}^{o} = \dot{\lambda}^{o} \partial_{\tau} Q^{o} = \dot{\lambda}^{o} \xi \partial_{\tau} \overline{\tau}, \\
\dot{\kappa}^{o} = \dot{\lambda}^{o} \partial_{\mu^{o}} Q^{o} = -\dot{\lambda}^{o} \xi.
\end{cases}$$
(2.33)

Flow rules associated with forward phase transformation.— Assuming

$$Q_f^t(\boldsymbol{\tau}, p, \mu^t) \equiv H\bar{\sigma} + p - \mu^t - Y^t, \tag{2.34}$$

where Y^t is a strictly positive scalar, the transformation related internal state variables are given by

$$\begin{cases}
\mathring{\mathbf{h}}^{t} = \dot{\lambda}_{f}^{t} \partial_{\tau} Q_{f}^{t} = \dot{\lambda}_{f}^{t} H \partial_{\tau} \bar{\tau}, \\
\dot{\xi} = \dot{\lambda}_{f}^{t} \partial_{p} Q_{f}^{t} = \dot{\lambda}_{f}^{t}, \\
\dot{\kappa}^{t} = \dot{\lambda}_{f}^{t} \partial_{\mu^{t}} Q_{f}^{t} = -\dot{\lambda}_{f}^{t},
\end{cases} (2.35)$$

or

$$\begin{cases} \mathring{\mathbf{h}}^t = \dot{\xi} H \partial_{\tau} \bar{\tau}, \\ \dot{\kappa}^t = -\dot{\xi}. \end{cases}$$
 (2.36)

Flow rules associated with reverse phase transformation.— Assuming

$$Q_r^t \left(\boldsymbol{\tau}, \boldsymbol{\mu}^t \right) \equiv -\frac{\boldsymbol{\tau} : \mathbf{h}^{in}}{\xi} - p + \boldsymbol{\mu}^t - Y^t, \tag{2.37}$$

the flow rules for reverse phase transformation are given by

$$\begin{cases}
\mathbf{\hat{h}}^{in} = \dot{\lambda}_r^t \partial_{\tau} Q_r^t = -\dot{\lambda}_r^t \frac{\mathbf{h}^{in}}{\xi}, \\
\dot{\xi} = \dot{\lambda}_r^t \partial_p Q_r^t = -\dot{\lambda}_r^t, \\
\dot{\kappa}^t = \dot{\lambda}_r^t \partial_{\mu^t} Q_r^t = \dot{\lambda}_r^t,
\end{cases} (2.38)$$

or equivalently by

$$\begin{cases}
\dot{\mathbf{h}}^{in} = \frac{\dot{\xi}}{\xi} \mathbf{h}^{in}, \\
\dot{\kappa}^t = -\dot{\xi}.
\end{cases}$$
(2.39)

Thus, it is assumed that the direction of the inelastic strain recovery is governed by the average direction of the martensite variants and the magnitude of its rate is proportional to the rate of martensite volume fraction so that there can be no inelastic strain whenever the martensite volume fraction is zero and *vice versa*.

Hardening functions associated with phase transformation and orientation.— The branched hardening function that changes with transformation direction, introduced in [114], is adopted for phase transformation

$$\mu^{t}(\kappa^{t}) = \mu^{t}(\xi) := \begin{cases} \frac{1}{2}a_{1}^{t} \left[1 + \xi^{n_{1}^{t}} - (1 - \xi)^{n_{2}^{t}} \right] + a_{3}^{t}; & \dot{\xi} > 0, \\ \frac{1}{2}a_{2}^{t} \left[1 + \xi^{n_{3}^{t}} - (1 - \xi)^{n_{4}^{t}} \right] - a_{3}^{t}; & \dot{\xi} < 0, \end{cases}$$
(2.40)

which allows for the experimentally observed asymmetry in forward and reverse phase transformation and for smooth transitions between the elastic and phase transformation regimes. The coefficients $a_1^t - a_3^t$ are material parameters while the exponents $n_1^t - n_4^t$, which take values in the interval (0,1], do not have an associated material property but are directly chosen to best fit the four corners of the transformation hysteresis plots.

A similar power-law form for the hardening function associated with orientation is introduced [113]

$$\mu^{o}(\kappa^{o};\xi) = \mu^{o}(\xi H;\xi) := \frac{1}{2}a_{1}^{o} \left\{ 1 + \left(\frac{H}{H^{\max}}\right)^{n_{1}^{o}} - \left[1 - \left(\frac{H}{H^{\max}}\right)\right]^{n_{2}^{o}} \right\}, \tag{2.41}$$

where a_1^o is a material parameter and $0 < n_1^o \le 1$, $0 < n_2^o \le 1$ are chosen to best fit the transitions between the elastic and orientation regimes.

Yield functions.— The dissipation inequalities (2.30) now read as

$$\begin{cases}
D^{o} = \dot{\lambda}^{o} \xi \left\{ \boldsymbol{\tau} : \partial_{\boldsymbol{\tau}} \left(\bar{\tau} \right) - \mu^{o} \right\} \geq 0; & \dot{\mathbf{h}}^{o} > \mathbf{0}, \\
D^{t} = \begin{cases}
\dot{\xi} \left\{ H \boldsymbol{\tau} : \partial_{\boldsymbol{\tau}} \left(\bar{\tau} \right) + p - \mu^{t} \right\} \geq 0; & \dot{\xi} > 0, \\
\dot{\xi} \left\{ \frac{\boldsymbol{\tau} : \dot{\mathbf{h}}^{in}}{\xi} + p - \mu^{t} \right\} \geq 0; & \dot{\xi} < 0, \\
D^{c} \equiv 0.
\end{cases} (2.42)$$

Given the convexity of the potential functions Q^o , Q_f^t , and Q_r^t , the following yield functions are assumed that satisfy the above dissipation inequalities

$$\begin{cases}
\Phi^{o}(\tau, \mu^{o}) = Q^{o}(\tau, \mu^{o}) = \bar{\tau} - \mu^{o} - Y^{o} \leq 0, \\
\Phi^{t}_{f}(\tau, p, \mu^{t}) = (1 - C)H\bar{\tau} + p - \mu^{t} - Y^{t} \leq 0, \\
\Phi^{t}_{r}(\tau, p, \mu^{t}) = -\left[(1 + C)\frac{\boldsymbol{\tau} \cdot \mathbf{h}^{in}}{\xi} + p - \mu^{t} \right] - Y^{t} \leq 0.
\end{cases} (2.43)$$

Note that $\Phi_f^t(\boldsymbol{\tau}, p, \mu^t) < Q_f^t(\boldsymbol{\tau}, p, \mu^t)$ and $\Phi_r^t(\boldsymbol{\tau}, p, \mu^t) < Q_r^t(\boldsymbol{\tau}, p, \mu^t)$, where the introduced parameter 0 < C < 1 in the expressions of Φ_f^t and Φ_r^t accounts for the dissimilar slopes of the transformation boundaries on the SMA phase diagram.

2.3.4 Tension/compression asymmetry in stiffness degradation, prevention of interpenetration of the crack faces, and crack irreversibility

In an effort to prohibit crack propagation under compression, only the tensile part of the elastic strain energy density, $W_{\mathbf{h}^e}^+$, is assumed to serve as the driving force for crack growth, which is defined through the energy decomposition into a positive and a negative part, introduced by [40, 41],

$$W_{\mathbf{h}^e}^+ = \frac{1}{2}\lambda \langle \operatorname{tr} \mathbf{h}^e \rangle^2 + \mu \operatorname{tr} \left[(\mathbf{h}_e^+)^2 \right], \quad W_{\mathbf{h}^e}^- = \frac{1}{2}\lambda \left(\operatorname{tr} \mathbf{h}^e - \langle \operatorname{tr} \mathbf{h}^e \rangle \right)^2 + \mu \operatorname{tr} \left[(\mathbf{h}_e^-)^2 \right]$$
(2.44)

where

$$\mathbf{h}_{e}^{+} = \sum_{\alpha} \langle h_{\alpha} \rangle \mathbf{n}_{\alpha} \otimes \mathbf{n}_{\alpha}, \quad \mathbf{h}_{e}^{-} = \mathbf{h}^{e} - \mathbf{h}_{e}^{+}, \tag{2.45}$$

are the positive and negative components of the elastic strain tensor, respectively, defined through its spectral decomposition, $\mathbf{h}^e = \sum_{\alpha} h_{\alpha}^e \mathbf{n}_{\alpha} \otimes \mathbf{n}_{\alpha}$, where λ and μ are the Lamé constants, and

$$\langle x \rangle = \begin{cases} 0, & x < 0 \\ x, & x \ge 0. \end{cases}$$

Furthermore, the constitutive response (2.23) is modified to read

$$\boldsymbol{\tau} = m(c)\partial_{\boldsymbol{h}}W_{\boldsymbol{h}^{e}}^{+} + \partial_{\boldsymbol{h}}W_{\boldsymbol{h}^{e}}^{-} = m(c)\left[\lambda\langle\operatorname{tr}\mathbf{h}^{e}\rangle\boldsymbol{\delta} + 2\mu\mathbf{h}_{e}^{+}\right] + \left[\lambda\left(\operatorname{tr}\mathbf{h}^{e} - \langle\operatorname{tr}\mathbf{h}^{e}\rangle\right)\boldsymbol{\delta} + 2\mu\mathbf{h}_{e}^{-}\right],\tag{2.46}$$

in order to prevent the interpenetration of the crack faces. Similarly the driving force for phase transformation, p, given in (2.27), is modified to read

$$p = \frac{1}{2}m(c)\Delta\lambda\langle\operatorname{tr}\mathbf{h}^{e}\rangle^{2} + \Delta\mu\operatorname{tr}\left[(\mathbf{h}_{e}^{+})^{2}\right] + \frac{1}{2}\Delta\lambda\left(\operatorname{tr}\mathbf{h}^{e} - \langle\operatorname{tr}\mathbf{h}^{e}\rangle\right)^{2} + \Delta\mu\operatorname{tr}\left[(\mathbf{h}_{e}^{-})^{2}\right] - \rho_{0}\Delta c\left[T - T_{0} - T\ln\left(\frac{T}{T_{0}}\right)\right] + \rho_{0}\Delta s_{0}T - \Delta u_{0}. \quad (2.47)$$

Thus, (2.31) is now written as

$$\rho_0 \pi = -m'(c) \mathcal{H} - \frac{\mathcal{G}_c}{2\ell} c, \tag{2.48}$$

where the history functional, \mathcal{H} , which satisfies the Kuhn-Tucker conditions for loading and unloading

$$W_{h}^{+} - \mathcal{H} \le 0, \quad \dot{\mathcal{H}} \ge 0, \quad \dot{\mathcal{H}} \left(W_{h}^{+} - \mathcal{H} \right) = 0,$$
 (2.49)

is introduced to enforce crack irreversibility [40], i.e., $\dot{c} \geq 0$.

Note that due to Poisson's ratio effects, compressive stresses may still contribute to the increase of damage; other schemes to describe the tension/compression asymmetry in the stiffness degradation response are proposed in [115].

2.3.5 Strong-form, boundary-value problem

In summary, the strong-form, boundary-value problem of the constitutive response reads as

Mechanical Equilibrium (2.9). –

$$\nabla_{x} \cdot \tau + \rho_0 \mathbf{b} = 0, \tag{2.50}$$

Microforce Balance ((2.11), (2.25), (2.48)). -

$$2J\mathcal{G}_c \ell \, \nabla_x \cdot \partial_x c = m'(c)\mathcal{H} + \frac{\mathcal{G}_c^0}{2\ell} c, \tag{2.51}$$

Constitutive equations (2.46). –

$$\boldsymbol{\tau} = m(c) \left[\lambda \langle \operatorname{tr} \mathbf{h}^e \rangle \boldsymbol{\delta} + 2\mu \mathbf{h}_e^+ \right] + \left[\lambda \left(\operatorname{tr} \mathbf{h}^e - \langle \operatorname{tr} \mathbf{h}^e \rangle \right) \boldsymbol{\delta} + 2\mu \mathbf{h}_e^- \right], \tag{2.52}$$

Evolution equations ((2.33), (2.36), (2.39)).

$$\begin{cases}
\mathbf{\mathring{h}}^{o} = \dot{\lambda}^{o} \xi \partial_{\tau} \bar{\tau}, \\
\mathbf{\mathring{h}}^{t} = \dot{\xi} H \partial_{\tau} \bar{\tau}; & \dot{\xi} > 0, \\
\mathbf{\mathring{h}}^{in} = \dot{\xi} \frac{\mathbf{h}^{in}}{\xi}; & \dot{\xi} < 0,
\end{cases}$$
(2.53)

Yield surfaces (2.54). –

$$\begin{cases}
\Phi^{o} = \bar{\tau} - \mu^{o} - Y^{o} = 0, \\
\Phi^{t}_{f} = (1 - C)H\bar{\tau} + p - \mu^{t} - Y^{t} = 0, \\
\Phi^{t}_{r} = -\left[(1 + C)\frac{\boldsymbol{\tau} \cdot \mathbf{h}^{in}}{\xi} + p - \mu^{t} \right] - Y^{t} = 0,
\end{cases} (2.54)$$

where μ^{o} , p and μ^{t} are given in (2.41), (2.27), and (2.40), respectively.

The equilibrium equations are subject to the boundary conditions

Boundary Conditions. -

$$\begin{cases} \mathbf{u}|_{\partial \mathcal{Q}_{t}^{u}} = \bar{\mathbf{u}}, \\ \mathbf{\sigma} \cdot \mathbf{n}|_{\partial \mathcal{Q}_{t}^{t}} = \bar{\mathbf{t}}, \\ \frac{\partial c}{\partial \mathbf{x}} \cdot \mathbf{n}|_{\partial \mathcal{Q}_{t}} = 0, \end{cases}$$
(2.55)

where $\bar{\boldsymbol{u}}$ and $\bar{\mathbf{t}}$ are prescribed displacement and tractions on the Dirichlet, $\partial \mathcal{Q}_t^u$, and von Neumann, $\partial \mathcal{Q}_t^t$, boundaries, respectively $(\partial \mathcal{Q}_t = \overline{\partial \mathcal{Q}_t^u \cup \partial \mathcal{Q}_t^t})$ and $\emptyset = \partial \mathcal{Q}_t^u \cap \partial \mathcal{Q}_t^t$.

2.4 Damage Evolution in 1D Problem

To obtain an insight into the damage evolution, the solution of the 1D boundary-value problem is given in this section.

Assuming tensile stretching and in the absence of body forces, the strong form of the balance equations, (2.50) and (2.51), and the constitutive relation, (2.46), read as

$$\begin{cases}
\frac{\partial \tau}{\partial x} = 0, \\
2\mathcal{G}_c \ell \frac{\partial^2 c}{\partial x^2} = m'(c)\mathcal{H} + \frac{\mathcal{G}_c}{2\ell}c, \\
\tau = m(c)E(\xi)h^e
\end{cases} \tag{2.56}$$

Thus, τ is independent of the spatial variable, *i.e.*, τ is homogeneous, and ignoring the spatial derivatives of c and assuming $m(c) \equiv (1-c)^2$, (2.56) reduces to

$$\begin{cases}
\tau = (1 - c)^2 E(\xi) h^e, \\
c = \frac{2\mathcal{H}}{2\mathcal{H} + \frac{\mathcal{G}_c}{2\ell}}.
\end{cases}$$
(2.57)

Thus, the critical values of stress, strain and damage after which both the stress and damage decrease in value upon an increase in strain can be found as

$$\begin{cases}
\tau_c = \frac{9}{16} \sqrt{\frac{E(\xi)\mathcal{G}_c}{6\ell}}, \\
h_c^e = \sqrt{\frac{\mathcal{G}_c}{6\ell E(\xi)}}, \\
c_c = \frac{1}{4}.
\end{cases} (2.58)$$

The above expressions are the ones derived from the 1D problem of the phase-field description of brittle fracture (elastic materials) by replacing τ by σ , h_c^e by ε_c , and $E(\xi)$ by E [42]. Both the critical values of stress and elastic strain are dependent on transformation through the value of $E(\xi)$ while the critical value of the phase-field is independent of model and material parameters.

It should be noted that the model could be alternatively formulated by adopting a different crack density (and degradation) functional, whose generalized form reads as $\Gamma_c(c,\partial_{\boldsymbol{x}}c)=\frac{1}{w_0}\left[\frac{1}{\ell}w(c)+4\ell\left(\partial_{\boldsymbol{x}}c\cdot\partial_{\boldsymbol{x}}c\right)\right]$; $w_0=8\int_0^1\sqrt{w(s)}ds$, where $w(c)\in[0,1]$, subject to the constraints w(0)=0 and w(1)=1, is a function that governs the shape of the regularized profile of the phase field, and $w_0>0$ is a normalization constant, such that an elastic phase is included in the damage response [39] or the critical stress becomes independent of ℓ [57].

2.5 Numerical Implementation

The variational form of the boundary-value problem given above reads as: Given **b** and $\bar{\mathbf{t}}$, find $(\boldsymbol{u}, c) \in \mathcal{V}_u \times H^1(\mathcal{Q}_t)$, such that

$$\begin{cases}
\int_{\mathcal{Q}_{t}} \left[\boldsymbol{\tau} : \nabla \boldsymbol{v} - \rho_{0} \mathbf{b} \cdot \boldsymbol{v} \right] d\boldsymbol{x} - \int_{\partial \mathcal{Q}_{t}} \bar{\mathbf{t}} \cdot \boldsymbol{v} ds = 0, \\
\int_{\mathcal{Q}_{t}} \left[2J \mathcal{G}_{c} \ell \, \partial_{\boldsymbol{x}} c \cdot \partial_{\boldsymbol{x}} w + m'(c) \mathcal{H} w + \frac{\mathcal{G}_{c}^{0}}{2\ell} cw \right] d\boldsymbol{x} = 0
\end{cases} \tag{2.59}$$

for all $(\boldsymbol{v}, w) \in \mathcal{V}_u^0 \times H^1(\mathcal{Q}_t)$, where

$$\mathcal{V}_{u} = \left\{ \boldsymbol{u} \in H^{1}(\mathcal{Q}_{t}); \boldsymbol{u} \big|_{\partial \mathcal{Q}_{t}^{u}} = \bar{\boldsymbol{u}} \right\}, \quad \mathcal{V}_{u}^{0} = \left\{ \boldsymbol{u} \in H^{1}(\mathcal{Q}_{t}); \boldsymbol{u} \big|_{\partial \mathcal{Q}_{t}^{u}} = 0 \right\}.$$
 (2.60)

Following the Galerkin method and a usual finite-element approximation of the functional spaces of the weak form, the discretized version of the above equation can be solved by a single-pass staggered scheme [40] as follows.

Given the converged values $\{u_n, c_n, \mathcal{H}_n, \mathbf{h}_n^{in}, \kappa_n^o, \kappa_n^t\}$ at the *n*-increment and the predefined temperature value at the n+1-increment, T_{n+1} :

- 1. Compute c_{n+1} from the microforce balance equation using \mathcal{H}_n .
- 2. Compute u_{n+1} from the mechanical equilibrium equation using the Newton's method, which results in an iterative loop inside the global (top-level) loop of load incrementation. At every iteration during this loop, compute the stress corresponding to a change of the strain field through another iteration loop, the Closest Point Projection Return Mapping Algorithm [113], under the approximation

$$\begin{split} \boldsymbol{\tau}(\boldsymbol{u_{n+1}}, \mathbf{h}_{n+1}^{in}, T_{n+1}, c_{n+1}) \\ &= m(c_{n+1}) \Big\{ \lambda \operatorname{tr} \left[\mathbf{h}^e \left(\boldsymbol{u}_{n+1}, \mathbf{h}_{n+1}^{in}, T_{n+1}, c_{n+1} \right) \right] \boldsymbol{\delta} + 2\mu \mathbf{h}_e^+ \left(\boldsymbol{u}_{n+1}, \mathbf{h}_{n+1}^{in}, T_{n+1}, c_{n+1} \right) \Big\} \\ &+ \Big\{ \lambda \Big[\operatorname{tr} \mathbf{h}^e \left(\boldsymbol{u}_{n+1}, \mathbf{h}_{n+1}^{in}, T_{n+1}, c_{n+1} \right) - \langle \operatorname{tr} \mathbf{h}^e \left(\boldsymbol{u}_{n+1}, \mathbf{h}_{n+1}^{in}, T_{n+1}, c_{n+1} \right) \rangle \Big] \boldsymbol{\delta} + 2\mu \mathbf{h}_e^- \left(\boldsymbol{u}_{n+1}, \mathbf{h}_{n+1}^{in}, T_{n+1}, c_{n+1} \right) \Big\}, \end{split}$$

by pushing forward all tensorial state variables from the previous global iteration, \boldsymbol{a}_n , to the current configuration $\mathbf{R}_{n+1}^{LT} \left(\mathbf{R}_n^L \boldsymbol{a}_n \mathbf{R}_n^{LT} \right) \mathbf{R}_{n+1}^L$, where \mathbf{R}^L is updated in closed form as described in [113], [116] (pp. 91-92), [117] (pp. 297).

3. Determine the history variable

$$\mathcal{H}_{n+1} = \begin{cases} W_{\boldsymbol{h}}^{+} \left(\boldsymbol{u_{n+1}}, \mathbf{h}_{n+1}^{in}, T_{n+1}, c_{n+1} \right), & W_{\boldsymbol{h}}^{+} \left(\boldsymbol{u_{n+1}}, \mathbf{h}_{n+1}^{in}, T_{n+1}, c_{n+1} \right) > \mathcal{H}_{n}, \\ \mathcal{H}_{n}, & \text{otherwise}, \end{cases}$$

The above algorithm is implemented in ABAQUS suite by exploiting the analogy between the microforce balance and heat transfer equations via a UMAT and a HETVAL subroutine [118, 119]. The above implementation is conditionally stable and requires the load increments employed to be sufficiently small [48, 120–122]. A comparison between the staggered and monolithic ABAQUS implementations can be found in [119].

3 Results

The calibration of the constitutive model regarding phase transformation and orientation is described in detail in [113]. The fracture toughness can be calibrated by compact-tension experiments as described in [36, 107] while the length scale parameter ℓ should be selected with consideration of the size of the domain/mesh of potential simulations and the ultimate tensile strength of the material [40, 42]. The simulations presented below are based on the model parameters given in Table 3.1. It should be noted that the fracture energy is amplified in simulations based on the finite element discretization; a scaled fracture toughness, e.g., $G_c^s = G_c/[1 + h_d/(4\ell)]$, where h_d is the minimum mesh size $(h_d = \sqrt{A} \text{ (or } \sqrt[3]{A})$ is the area (or volume) of an element), could be used in the simulations instead [124]. For the examples below, the domains along the crack path are discretized such that $h_d < \ell/3$.

Table 3.1: Parameter values used in the simulations.

(a) Elastic constants

parameter	value
E_A [MPa]	74000
$ u_A$	0.33
E_M [MPa]	62000
$ u_M$	0.33

(b) Phase transformation/Orientation parameters

parameter	value	parameter	value
M_s [K]	340	H_{max}	0.06
M_f [K]	320	n_1^t	1
A_s [K]	367	$n_2^{ar{t}}$	1
A_f [K]	379	$n_3^{\overline{t}}$	1
$C_A \text{ [MPa K}^{-1}]$	8	$n_4^{ otag}$	1
$C_M [\mathrm{MPa} \ \mathrm{K}^{-1}]$	15	n_1^0	1
Y^0 [MPa]	190	n_2^0	1
$a_1^0 \text{ [MPa]}$	220	-	

(c) Phase-field parameters

parameter	value
$\ell \text{ [mm]}$ $\mathcal{G}_c \text{ [MPa.mm]}$	0.6 128

3.1 Uniaxial Isothermal & Isobaric Loading

The constitutive material response is depicted first by simulations performed under uniaxial isothermal and isobaric conditions. The uniaxial isothermal stress–strain response at three different temperatures is shown in Figure 3.1. At T=298 K, the material is initially in a self-accommodated martensite state and undergoes orientation of martensite variants upon loading while at T=353 K, the material is initially in the austenite phase and undergoes stress-induced phase transformation (Figure 3.1a). At T=385 K, the material displays a superelastic response upon unloading (during unloading c remains constant). Note that in these simulations and all that follow no reverse phase transformation is permitted for $c>c_c=1/4$. The isobaric strain–temperature response under three bias load levels is shown in Figure 3.2. Under $\sigma=0$ MPa, the material, initially in the austenite phase, transforms to self-accommodated martensite, under $\sigma=200$ MPa, to a mixture of self-accommodated and oriented martensite, and under $\sigma=300$ MPa, to oriented martensite. Note the difference in the transformation strain value between the three simulations. From the simulations, it is apparent that the model accounts for reversible phase transformation from austenite to self-accommodated and/or oriented martensite, orientation of martensite variants, and can address the deformation response in the concurrent presence of several phases, *i.e.*, austenite, self-accommodated and oriented martensite.

3.2 Stable Crack Growth under Actuation

In this section, the model's ability to reproduce the experimentally observed crack growth under "actuation" loading conditions is demonstrated. The numerical simulations are performed on an infinite center-cracked SMA plate subjected to uniform cooling from T = 400 K, with $\Delta T = 4 \times 10^{-3}$ K, under a far-field constant uniaxial tensile load applied in the perpendicular to the crack plane direction, $\sigma_{\infty} = 280$ MPa. Due to symmetry, one quarter of the plate is discretized by 53,340 eight-noded quadrilateral plane-strain elements with reduced integration. The far-field stress level is chosen to be low enough for the crack

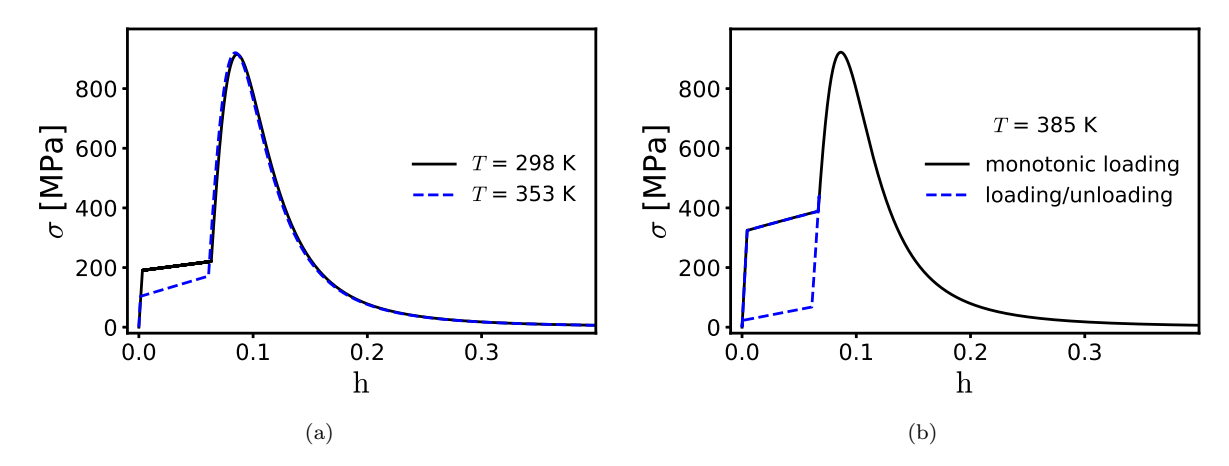


Fig. 3.1: Stress-strain response under uniaxial isothermal loading (a) at T = 298 K and T = 353 K and (b) at T = 385 K.

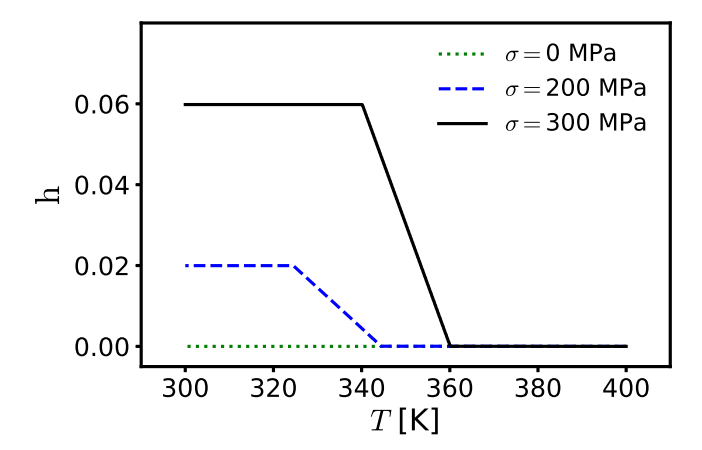


Fig. 3.2: Strain-temperature response under isobaric conditions.

to propagate due to mechanical loading alone but high enough for the crack to grow during cooling. As already discussed in [30], stress redistribution due to large-scale transformation occurring in regions "in front" of the crack tip results in raising the driving force for crack growth, *i.e.*, the elastic strain energy density (see Figure 3.3), while stress redistribution due to transformation left in the wake of the crack ("behind" the crack tip) as crack advances results in crack shielding and, therefore, in stable crack growth. That is phase transformation affects both the driving force for crack growth and the crack growth kinetics due to the induced stress redistribution that facilitates crack growth when occurring in a fan in front of the crack tip and shields the crack when occurring behind this fan. The martensite volume fraction, ξ , and damage, c, distributions at the initiation of crack advance and during crack growth are shown in Figure 3.4. The normalized temperature, $[C_M(T-M_S)]/\sigma_{\infty}$, versus the normalized crack length, $\Delta a/a_0$, plot in Figure 3.5, where Δa is the crack extension and a_0 is the initial half crack length, shows the resulting resistance ("R-curve"-type) response. The normalization chosen is the one proposed in [125].

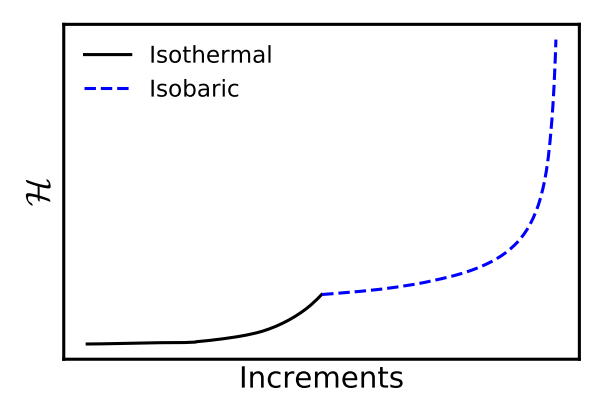


Fig. 3.3: Driving force for damage, \mathcal{H} , at the crack tip of the infinite center-cracked plate subjected to cooling under a constant far-field load applied in the perpendicular to the crack plane direction. The solid line represents the evolution of the driving force during the isothermal application of the bias load, $\sigma_{\infty} = 280$ MPa, at T = 400 K and the dashed line the subsequent evolution during cooling while the bias load remains constant.

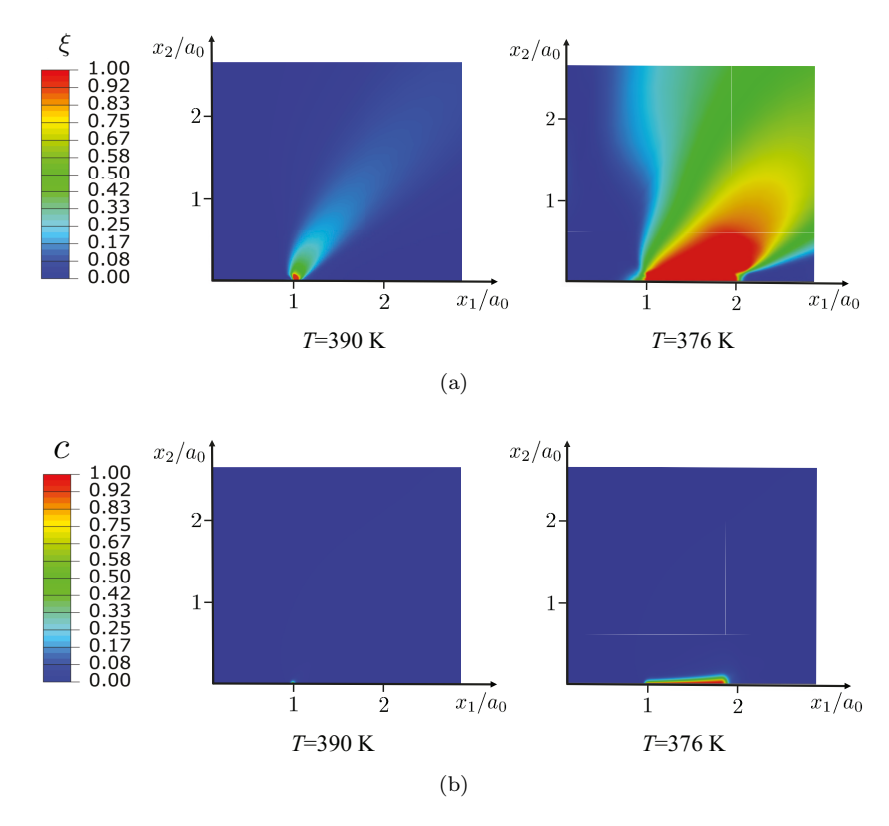


Fig. 3.4: Martensite volume fraction, ξ , (a) and damage, c, (b) distributions on the infinite center-cracked plate subjected to cooling under a constant far-field load applied in the perpendicular to the crack plane direction at T=390 K, which corresponds to initiation of crack advance, and during crack growth at T=376 K.

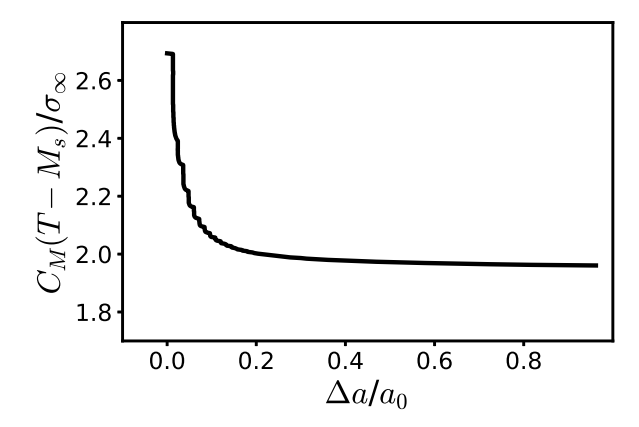


Fig. 3.5: Crack growth resistance for the infinite center-cracked plate subjected to cooling under a constant far-field load applied in the perpendicular to the crack plane direction.

3.3 3D crack growth simulations

The efficiency of the numerical implementation of the model is verified by crack growth simulations in 3D complex geometries resulting in mixed-mode fracture.

The fracture response of a 3D notched plate is simulated with the notch inclined along the thickness under both isothermal and actuation loading conditions. The geometric configuration has been adopted from [46]. In the isothermal simulation, a displacement of 4 mm is applied, with a fixed increment of $\Delta u=10^{-3}mm$, at T=353 K on the bearing surface of the upper pin hole while bearing surface of the lower pin hole is kept fixed. The third hole is traction free, placed with an offset from the center so as to induce mixed-mode fracture conditions. A total of 100,943 linear tetrahedral elements are used for discretizing the whole domain. The martensite volume fraction, ξ , evolution and crack growth pattern at different stages of loading are shown in Figure 3.6. The force generated at the pin holes is plotted against the applied displacement in Figure 3.6b. The crack front progressively turns, propagates in a stable manner and eventually becomes perpendicular to the free surface. In another simulation, a constant load of F = 90 KN is applied on the bearing surface of the upper pin hole at T = 400 K keeping the lower pin hole fixed. The plate is then cooled with $\Delta T = 8 \times 10^{-3}$ K. The martensite volume fraction, ξ , evolution and crack growth pattern at different stages of cooling are shown in Figure 3.7. The resulting displacement-temperature curve is shown in Figure 3.7b. The crack starts growing stably at $T=395.1~\mathrm{K}$. During cooling, the resulting large-scale phase transformation promotes crack advance leading to an unstable crack growth at T = 390.6 K.

Lastly, the fracture response of a SMA torque tube is simulated under torque at T=353 K. An initial through thickness circumferential notch is assumed. A rotation θ about the longitudinal axis is applied, with a fixed $\Delta\theta=4\times10^{-4}$ rad, on one end of the tube while the other end is kept fixed. The crack pattern at different stages of loading is shown in Figure 3.8. Two cracks start propagating spirally from the initial notch and eventually merge with each other splitting the tube into three pieces.

Conclusions

A finite-strain, phase-field description of the fracture response of shape memory alloys (SMAs) is presented. The finite-strain formulation is based on the Eulerian logarithmic strain, the objective logarithmic rate and the additive decomposition of the rate of deformation, and the phase-field one on a postulated microforce balance equation. Based on experimental observations and numerical simulations, it is assumed that fracture is stress-driven and only the elastic strain energy contributes to the driving force for crack formation and growth, *i.e.*, the work of inelastic deformation (orientation of martensite variants or phase

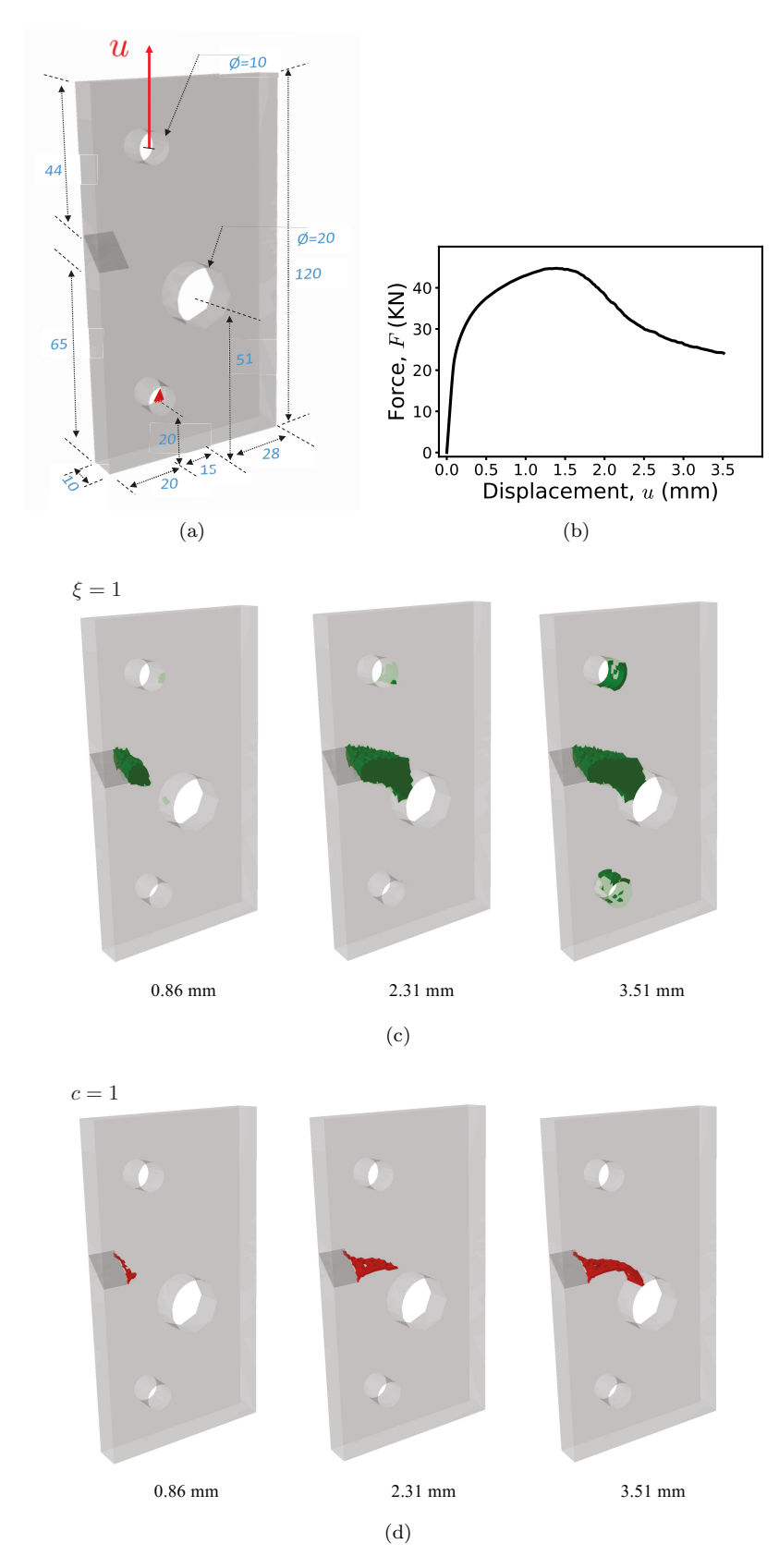


Fig. 3.6: Fracture of a 3D notched plate under isothermal loading condition at T=353 K. (a) Geometry and boundary conditions. All measures given are in mm. (b) Force–displacement curve at a pin hole up to crack reaching the traction-free hole. (c) Martensite volume fraction, ξ , evolution (iso-surfaces of $\xi=1$) and (d) crack pattern (iso-surfaces of c=1) at three applied displacement values.

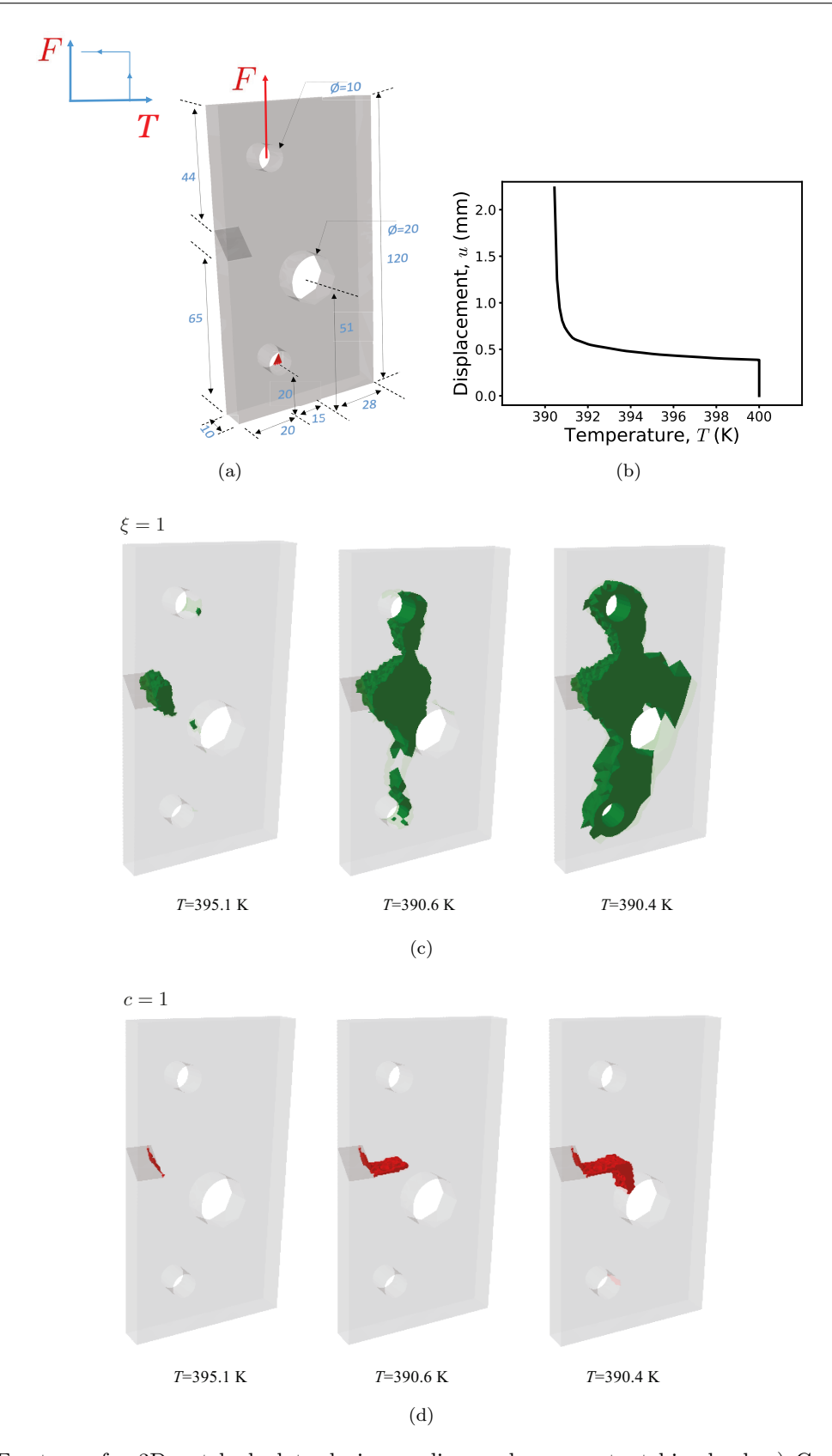


Fig. 3.7: Fracture of a 3D notched plate during cooling under a constant bias load. a) Geometry and boundary conditions. All measures given are in mm. (b) Displacement–temperature curve at a pin hole up to crack reaching the traction-free hole. (c) Iso-surfaces of $\xi = 1$, at three different temperatures. (d) Iso-surfaces of c = 1 at three different temperatures.

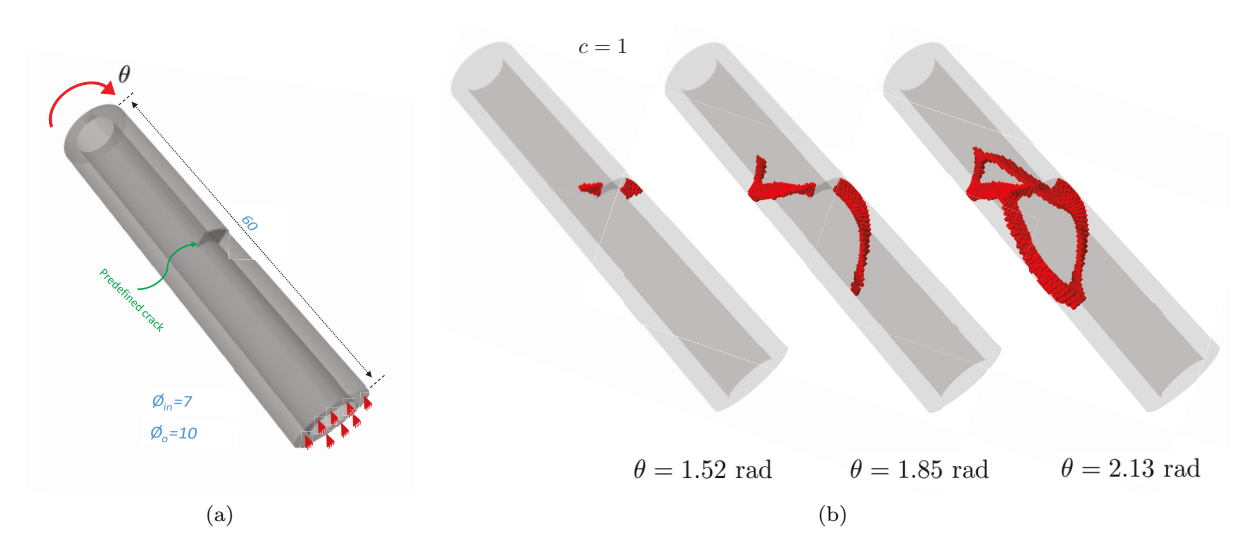


Fig. 3.8: Fracture of a torque tube under isothermal torsion at T = 353 K. (a) Geometry and boundary conditions. All measures given are in mm. (b) Crack pattern at different stages of loading.

transformation) is assumed to have a negligible contribution to the evolution of the intrinsic damage mechanisms at the fracture process zone. The model is shown able to reproduce experimental observations on the fracture response of SMAs, such as (i) isothermal orientation and phase transformation toughening, i.e., stable crack growth under isothermal loading of an SMA in an initially self-accommodated martensite state or in austenite at a temperature below M_d , and (ii) initiation of crack advance and subsequent stable crack growth during cooling of an SMA in the austenite sate under a sufficiently high bias load level (termed actuation loading). The model and its numerical implementation are further verified by simulations of complex 3D structures under isothermal and actuation loading conditions. The proposed phase field framework to fracture in SMAs, envisioned to facilitate optimum design of SMA components, could be augmented to describe e.g., reorientation, tension-compression asymmetry, minor loops, plastic deformation, and latent heat effects.

Acknowledgements

This study was supported by the National Science Foundation under Grant no. CMMI-1917441. The authors acknowledge the Research Computing Data Core (RCDC) at the University of Houston for the supercomputing resources made available for conducting the research reported in this paper.

References

- 1. S. Miyazaki. Engineering Aspects of Shape Memory Alloys. Butterworth-Heinemann, London, 1990.
- 2. K. Otsuka and C.M. Wayman, editors. Shape Memory Materials. Cambridge University Press, Cambridge, 1999.
- 3. N.B. Morgan. Medical shape memory alloy applications the market and its products. *Mater. Sci. Eng. A.*, 378: 16–23, 2004.
- 4. D.C. Lagoudas, editor. Shape Memory Alloys: Modelling and Enginnering Applications. Springer, New-York, 2008.
- 5. S. Barbarino, E.S. Flores, R.M. Ajaj, I. Dayyani, and M.I. Friswell. A review on shape memory alloys with applications to morphing aircraft. *Smart Mater. Struct.*, 23(6):063001, 2014.
- J.M. Jani, M. Leary, A. Subic, and M.A. Gibson. A review of shape memory alloy research, applications and opportunities. *Mater. Design.*, 56:1078–1113, 2014.
- S.W. Robertson, A. Metha, A.R. Pelton, and R.O. Ritchie. Evolution of crack-tip transformation zones in superelastic Nitinol subjected to in situ fatigue: A fracture mechanics and synchrotron X-ray micro-diffraction analysis. Acta Mater., 55:6198–6207, 2007.
- 8. S. Gollerthan, M.L. Young, A. Baruj, J. Frenzel, W.W. Schmahl, and G. Eggeler. Fracture mechanics and microstructure in NiTi shape memory alloys. *Acta Mater.*, 57:1015–1025, 2009.
- S.W. Robertson, A.R. Pelton, and R.O. Ritchie. Mechanical fatigue and fracture of Nitinol. Int. Mater. Rev., 57(1): 1–36, 2012.
- T. Baxevanis and D.C. Lagoudas. Fracture mechanics of shape memory alloys: review and perspectives. Int. J. Fract., 191:191–213, 2015.
- G. Stam and E. van der Giessen. Effect of reversible phase transformations on crack growth. Mech. Mater., 21:51-71, 1995.
- 12. S. Yi and S. Gao. Fracture toughening mechanism of shape memory alloys due to martensite transformation. *Int. J. Solids Struct.*, 37:5315–5327, 2000.
- 13. S. Yi, S. Gao, and S. Shen. Fracture toughening mechanism of shape memory alloys under mixed-mode loading due to martensite transformation. *Int. J. Solids Struct.*, 38:4463–4476, 2001.
- 14. G.Z. Wang. Effect of martensite transformation on fracture behavior of shape memory alloy NiTi in a notched specimen. *Int. J. Fract.*, 146:93–104, 2007.
- G.Z. Wang. A finite element analysis of evolution of stress-strain and martensite transformation in front of a notch in shape memory alloy NiTi. *Mater. Sci. Engng. A.*, 460–461:460–461, 2007.
- Y. Freed and L. Banks-Sills. Crack growth resistance of shape memory alloys by means of a cohesive zone model. J. Mech. Phys. Solids, 55:2157–2180, 2007.
- C. Maletta and F. Furgiuele. Analytical modeling of stress-induced martensitic transformation in the crack tip region of nickel-titanium alloys. Acta Mater., 58:92–101, 2010.
- C. Maletta. A novel fracture mechanics approach for shape memory alloys with trilinear stress-strain behavior. Int. J. Fract., 177(1):39-51, 2012.
- T. Baxevanis and D.C. Lagoudas. A mode I fracture analysis of a center-cracked infinite shape memory alloy plate under plane stress. *Int. J. Fract.*, 175(2):151–166, 2012.
- T. Baxevanis, Y. Chemisky, and D.C. Lagoudas. Finite element analysis of the plane-strain crack-tip mechanical fields in pseudoelastic shape memory alloys. Smart Mater. Struct., 21(9):094012, 2012.
- G. Özerim, G. Anlaş, and Z. Moumni. On crack tip stress fields in pseudoelastic shape memory alloys. Int. J. Fract., 212(2):205–217, 2018.
- 22. T. Baxevanis, C.M. Landis, and D.C. Lagoudas. On the fracture toughness of pseudoelastic shape memory alloys. *J. Appl. Mech. –T ASME*, 81:041005, 2013.
- 23. S. Hazar, W. Zaki, Z. Moumni, and G. Anlas. Modeling of steady-state crack growth in shape memory alloys using a stationary method. *Int. J. Plastic.*, 67:26–38, 2015.
- 24. D. Jiang and C.M. Landis. A constitutive model for isothermal pseudoelasticity coupled with plasticity. Shape Mem. Super., 2(4):360–370, 2016.
- 25. W. Yan, C.H. Wang, X.P. Zhang, and Y.W. Mai. Effect of transformation volume contraction on the toughness of superelastic shape memory alloys. *Smart Mater. Struct.*, 11:947–955, 2002.
- 26. T. Baxevanis, A. Parrinello, and D.C. Lagoudas. On the fracture toughness enhancement due to stress-induced phase transformation in shape memory alloys. *Int. J. Plast.*, 50:158–169, 2013.
- S. Jape, T. Baxevanis, and D.C. Lagoudas. On the fracture toughness and stable crack growth in shape memory alloy
 actuators in the presence of transformation-induced plasticity. *Int. J. Fract.*, 209:117–130, 2017.
- 28. T. Baxevanis, C.M. Landis, and D.C. Lagoudas. On the effect of latent heat on the fracture toughness of pseudoelastic shape memory alloys. *J. Appl. Mech.*, *Transactions ASME*, 81(10), 2014. doi: 10.1115/1.4028191.
- 29. Y. You, X. Gu, Y. Zhang, Z. Moumni, G. Anlaş, and W. Zhang. Effect of thermomechanical coupling on stress-induced martensitic transformation around the crack tip of edge cracked shape memory alloy. *Int. J. Fract.*, 216(1):123–133, 2019.
- 30. T. Baxevanis, A. Parrinello, and D.C. Lagoudas. On the driving force for crack growth during thermal actuation of shape memory alloys. *J. Mech. Phys. Solids*, 89:255–271, 2016.
- 31. A. Illiopoulos, J. Steuben, T. Kirk, T. Baxevanis, J. Michopoulos, and D.C. Lagoudas. Thermomechanical failure response of notched NiTi coupons. *Int. J. Solids Struct.*, 125:265–275, 2017.
- 32. S. Jape, T. Baxevanis, and D.C. Lagoudas. Stable crack growth during thermal actuation of shape memory alloys. Shape Mem. Super., 2(1):104–113, 2016.

- 33. K. Gall, N. Yang, H. Sehitoglu, and Y. I. Chumlyakov. Fracture of precipitated NiTi shape memory alloys. *Int. J. Fract.*, 109:189–207, 1998.
- J.S. Olsen, Z.L. Zhang, H. Lu, and C. van der Eijk. Fracture of notched round-bar NiTi-specimens. Engng. Fract. Mech., 84:1 – 14, 2012.
- 35. M.M. Hasan and T. Baxevanis. Structural fatigue and fracture of shape memory alloy actuators: Current status and perspectives. J. Intell. Mater. Syst. Struc., 33(12):1475-1486, 2022.
- J. Makkar and T. Baxevanis. Notes on the experimental measurement of fracture toughness of shape memory alloys.
 J. Intel. Mater. Sys. Struct., page 1045389X19888730, 2019. doi: 10.1177/1045389X19888730.
- 37. T. Ungàr, J. Frenzel, S. Gollerthan, G. Ribárik, L. Balogh, and G. Eggeler. On the competition between the stress-induced formation of martensite and dislocation plasticity during crack propagation in pseudoelastic niti shape memory alloys. J. Mater. R., 32(23):4433–4442, 2017. doi: 10.1557/jmr.2017.267.
- 38. B. Bourdin, G.A. Francfort, and J.J. Marigo. Numerical experiments in revisited brittle fracture. *J. Mech. Phys. Solids*, 48(4):797–826, 2000.
- 39. G.A. Francfort and J.J. Marigo. Revisiting brittle fracture as an energy minimization problem. *J. Mech. Phys. Solids*, 46(8):1319–1342, 1998.
- 40. C. Miehe, M. Hofacker, and F. Welschinger. A phase field model for rate-independent crack propagation: Robust algorithmic implementation based on operator splits. Comp. Meth. Appl. Mech. Engng., 199(45–48):2765–2778, 2010.
- 41. C. Miehe, F. Welschinger, and M. Hofacker. Thermodynamically consistent phase-field models of fracture: Variational principles and multi-field FE implementations. *Int. J. Num. Meth. Engng.*, 83(10):1273–1311, 2010.
- 42. M.J. Borden, C.V. Verhoosel, M.A. Scott, T.J.R. Hughes, and C.M. Landis. A phase-field description of dynamic brittle fracture. Comp. Meth. Appl. Mech. Engng., 217–220:77–95, 2012.
- M.J. Borden, T.J.R. Hughes, C.M. Landis, and C.V. Verhoosel. A higher-order phase-field model for brittle fracture: Formulation and analysis within the isogeometric analysis framework. Comp. Meth. Appl. Mech. Engng., 273:100–118, 2014
- 44. C. Kuhn and R. Müller. A continuum phase field model for fracture. Eng. Fract. Mech., 77(18):3625-3634, 2010.
- 45. P. Shanthraj, B. Svendsen, L. Sharma, F. Roters, and D. Raabe. Elasto-viscoplastic phase field modelling of anisotropic cleavage fracture. *J. Mech. Phys. Solids*, 99:19–34, 2017.
- 46. M. Ambati, T. Gerasimov, and L. De Lorenzis. A review on phase-field models of brittle fracture and a new fast hybrid formulation. *Comp. Mech.*, 55(2):383–405, 2014.
- K.D. Nguyen, C.L. Thanh, F. Vogel, H. Nguyen-Xuan, and M. Abdel-Wahab. Crack propagation in quasi-brittle materials by fourth-order phase-field cohesive zone model. Th. Appl. Fract. Mech., 118:103236, 2022.
- 48. O. Lampron, D. Therriault, and M. Lévesque. An efficient and robust monolithic approach to phase-field quasi-static brittle fracture using a modified newton method. *Comp. Meth. Appl. Mech. Engng.*, 386:114091, 2021.
- 49. T. Gerasimov and L. De Lorenzis. Second-order phase-field formulations for anisotropic brittle fracture. Comp. Meth. Appl. Mech Engng., 389:114403, 2022.
- 50. L. Novelli, L. Gori, and R.L. da Silva Pitangueira. Phase-field modelling of brittle fracture with smoothed radial point interpolation methods. *Engng. Analys. Bound. Elem.*, 138:219–234, 2022.
- 51. E. Tanné, T. Li, B. Bourdin, J.J. Marigo, and C. Maurini. Crack nucleation in variational phase-field models of brittle fracture. J. Mech. Phys. Solids, 110:80–99, 2018.
- L. Yang, Y. Yang, H. Zheng, and Z. Wu. An explicit representation of cracks in the variational phase field method for brittle fractures. Comp. Meth. Appl. Mech. Engng., 387:114127, 2021.
- 53. T.K. Mandal, V.P. Nguyen, and J.Y. Wu. Length scale and mesh bias sensitivity of phase-field models for brittle and cohesive fracture. *Engng. Fract. Mech.*, 217:106532, 2019.
- T. Xue, S. Adriaenssens, and S. Mao. Mapped phase field method for brittle fracture. Comp. Meth. Appl. Mech. Enang., 385:114046, 2021.
- 55. K. Yun, M.H. Kim, and P.H. Chu. A modified phase field model for predicting the fracture behavior of quasi-brittle materials. *Int. J. Num. Meth. Engng.*, 122(20):5656–5675, 2021.
- 56. B. Li, C. Peco, D. Millán, I. Arias, and M. Arroyo. Phase-field modeling and simulation of fracture in brittle materials with strongly anisotropic surface energy. *Int. J. Num. Meth. Engng.*, 102(3-4):711–727, 2015.
- J.Y. Wu. A unified phase-field theory for the mechanics of damage and quasi-brittle failure. J. Mech. Phys. Solids, 103:72–99, 2017.
- M.J. Borden, T.J.R. Hughes, C.M. Landis, A. Anvari, and I.J. Lee. A phase-field formulation for fracture in ductile materials: Finite deformation balance law derivation, plastic degradation, and stress triaxiality effects. Comp. Meth. Appl. Mech. Engng., 312:130–166, 2016.
- 59. C. Miehe, F. Aldakheel, and A. Raina. Phase field modeling of ductile fracture at finite strains: A variational gradient-extended plasticity-damage theory. *Int. J. Plast.*, 2016. Article in Press.
- 60. C. Miehe, D. Kienle, F. Aldakheel, and S. Teichtmeister. Phase field modeling of fracture in porous plasticity: A variational gradient-extended eulerian framework for the macroscopic analysis of ductile failure. Comp. Meth. Appl. Mech. Engng., 312:3–50, 2016.
- 61. C. Miehe, M. Hofacker, L.M. Schänzel, and F. Aldakheel. Phase field modeling of fracture in multi-physics problems. Part II. Coupled brittle-to-ductile failure criteria and crack propagation in thermo-elastic-plastic solids. Comp. Meth. Appl. Mech. Engng., 294:486–522, 2015.
- M. Ambati, T. Gerasimov, and L. De Lorenzis. Phase-field modeling of ductile fracture. Com. Mech., 55(5):1017–1040, 2015.
- 63. Z. Tao, X. Li, S. Tao, and Z. Chen. Phase-field modeling of 3d fracture in elasto-plastic solids based on the modified gtn theory. *Engag. Fract. Mech.*, 260:108196, 2022.

64. F. Aldakheel, N. Noii, T. Wick, O. Allix, and P. Wriggers. Multilevel global—local techniques for adaptive ductile phase-field fracture. Comp. Meth. Appl. Mech. Engng., 387:114175, 2021.

- D. Proserpio, M. Ambati, L. De Lorenzis, and J. Kiendl. Phase-field simulation of ductile fracture in shell structures. Comp. Meth. Appl. Mech. Engng., 385:114019, 2021.
- 66. J. Han, S. Matsubara, S. Moriguchi, M. Kaliske, and K. Terada. Crack phase-field model equipped with plastic driving force and degrading fracture toughness for ductile fracture simulation. Comp. Mech., 69:151–175, 2022.
- 67. B. Talamini, M.R. Tupek, A.J. Stershic, T. Hu, J.W. Foulk, J.T. Ostien, and J.E. Dolbow. Attaining regularization length insensitivity in phase-field models of ductile failure. *Comp. Meth. Appl. Mech. Engng.*, 384:113936, 2021.
- 68. P.S. Ma, J.Y. Ye, K. Tian, X.H. Chen, and L.W. Zhang. Fracture phase field modeling of 3d stitched composite with optimized suture design. *Comp. Meth. Appl. Mech. Engng.*, 392:114650, 2022.
- X. Li and Y. Xu. Phase field modeling scheme with mesostructure for crack propagation in concrete composite. Int. J. Solids Struct., 234-235:111259, 2022.
- 70. Z.Z. Pan, L.W. Zhang, and K.M. Liew. A phase-field framework for failure modeling of variable stiffness composite laminae. Comp. Meth. Appl. Mech. Engng., 388:114192, 2022.
- 71. C. Miehe and L.M. Schänzel. Phase field modeling of fracture in rubbery polymers. Part I: Finite elasticity coupled with brittle failure. J. Mech. Phys. Solids, 65(1):93–113, 2014.
- 72. P.J. Loew, B. Peters, and L.A.A. Beex. Rate-dependent phase-field damage modeling of rubber and its experimental parameter identification. *J. Mech. Phys. Solids*, 127:266–294, 2019.
- 73. J. Wu, C. McAuliffe, H. Waisman, and G. Deodatis. Stochastic analysis of polymer composites rupture at large deformations modeled by a phase field method. Comp. Meth. Appl. Mech. Engng., 312:596-634, 2016.
- 74. M. Dinachandra and A. Alankar. Adaptive finite element modeling of phase-field fracture driven by hydrogen embrittlement. Comp. Meth. Appl. Mech. Engng., 391:114509, 2022.
- E. Martínez-Pañeda, A. Golahmar, and C.F. Niordson. A phase field formulation for hydrogen assisted cracking. Comp. Meth. Appl. Mech. Engng., 342:742-761, 2018.
- 76. Z.A. Wilson and C.M. Landis. Phase-field modeling of hydraulic fracture. J. Mech. Phys. Solids, 96:264-290, 2016.
- 77. S. Lee, A. Mikelić, M.F. Wheeler, and T. Wick. Phase-field modeling of proppant-filled fractures in a poroelastic medium. Comp. Meth. Appl. Mech. Engng., 312:509–541, 2016.
- S. Lee, M.F. Wheeler, and T. Wick. Pressure and fluid-driven fracture propagation in porous media using an adaptive finite element phase field model. Comp. Meth. Appl. Mech. Engag., 305:111–132, 2016.
- Y. Heider and B. Markert. A phase-field modeling approach of hydraulic fracture in saturated porous media. Mech. Res. Com., 2015. Article in Press.
- 80. J. Ulloa, J. Wambacq, R. Alessi, E. Samaniego, G. Degrande, and S. François. A micromechanics-based variational phase-field model for fracture in geomaterials with brittle-tensile and compressive-ductile behavior. *J. Mech. Phys. Solids*, 159:104684, 2022.
- 81. Y. Li, T. Yu, and S. Natarajan. An adaptive isogeometric phase-field method for brittle fracture in rock-like materials. *Engng. Fract. Mech.*, 263:108298, 2022.
- 82. H.S. Suh and W. Sun. Asynchronous phase field fracture model for porous media with thermally non-equilibrated constituents. Comp. Meth. Appl. Mech. Engng., 387:114182, 2021.
- 83. A. Spetz, R. Denzer, E. Tudisco, and O. Dahlblom. A modified phase-field fracture model for simulation of mixed mode brittle fractures and compressive cracks in porous rock. *Rock Mech. Rock Engng.*, 54:5375–5388, 2021.
- 84. F. Fei, J. Choo, C. Liu, and J.A. White. Phase-field modeling of rock fractures with roughness. Int. J. Num. Analyt. Meth. Geomech., 46(5):841–868, 2022.
- 85. S. Liu, Y. Wang, C. Peng, and W. Wu. A thermodynamically consistent phase field model for mixed-mode fracture in rock-like materials. *Comp. Meth. Appl. Mech. Engng.*, 392:114642, 2022.
- 86. S. Wang, J. Zhang, L. Zhao, and W. Zhang. Phase field modeling of anisotropic tension failure of rock-like materials. *Front. Phys.*, 9, 2021.
- 87. J.Y. Wu and W.X. Chen. Phase-field modeling of electromechanical fracture in piezoelectric solids: Analytical results and numerical simulations. Comp. Meth. Appl. Mech. Engng., 387:114125, 2021.
- M.M. Hasan and T. Baxevanis. A phase-field model for low-cycle fatigue of brittle materials. Int. J. Fat., 150:106297, 2021.
- M. Caputo and M. Fabrizio. Damage and fatigue described by a fractional derivative model. J. Comp. Phys., 293: 400–408, 2015.
- J.L. Boldrini, E.A. Barros de Moraes, L.R. Chiarelli, F.G. Fumes, and M.L. Bittencourt. A non-isothermal thermodynamically consistent phase field framework for structural damage and fatigue. Comp. Meth. Appl. Mech. Engng., 312:395–427, 2016.
- 91. G. Amendola, M. Fabrizio, and J.M. Golden. Thermomechanics of damage and fatigue by a phase field model. *J. Therm. Stresses*, 39:487–499, 2016.
- 92. R. Alessi, S. Vidoli, and L. De Lorenzis. A phenomenological approach to fatigue with a variational phase-field model: The one-dimensional case. *Engng. Fract. Mech.*, 190:53–73, 2018.
- 93. P. Carrara, M. Ambati, R. Alessi, and L. De Lorenzis. A framework to model the fatigue behavior of brittle materials based on a variational phase-field approach. *Comp. Meth. Appl. Mech. Engng.*, 361:112731, 2020.
- Y.S. Lo, M.J. Borden, K. Ravi-Chandar, and C.M. Landis. A phase-field model for fatigue crack growth. J. Mech. Phys. Solids, 132:103684, 2019.
- 95. P.J. Loew, B. Peters, and L.A.A. Beex. Fatigue phase-field damage modeling of rubber using viscous dissipation: Crack nucleation and propagation. *Mech. Mater.*, 142:103282, 2020.

- 96. A. Mesgarnejad, A. Imanian, and A. Karma. Phase-field models for fatigue crack growth. Th. Appl. Fract. Mech., 103:102282, 2019.
- 97. M. Seiler, T. Linse, P. Hantschke, and M. Kästner. An efficient phase-field model for fatigue fracture in ductile materials. *Engng. Fract. Mech.*, 224:106807, 2020.
- 98. J. Ulloa, J. Wambacq, R. Alessi, G. Degrande, and S. François. Phase-field modeling of fatigue coupled to cyclic plasticity in an energetic formulation. *Comp. Meth. Appl. Mech. Engng.*, 373:113473, 2021.
- G.A. Haveroth, M.G. Vale, M.L. Bittencourt, and J.L. Boldrini. A non-isothermal thermodynamically consistent phase field model for damage, fracture and fatigue evolutions in elasto-plastic materials. *Comp. Meth. Appl. Mech. Engng.*, 364:112962, 2020.
- 100. Z. Khalil, A.Y. Elghazouli, and E. Martínez-Pañeda. A generalised phase field model for fatigue crack growth in elastic-plastic solids with an efficient monolithic solver. Comp. Meth. Appl. Mech. Engng., 388:114286, 2022.
- I. Koutromanos, A. Tola-Tola, and M.R. Eatherton. Phase-field description of ductile fracture in structural steel under cyclic loading. J. Struct. Engng., 148:04022073, 2022.
- 102. S. Yan, C. Schreiber, and R. Müller. An efficient implementation of a phase field model for fatigue crack growth. *Int. J. Fract.*, 2022.
- K. Seleš, F. Aldakheel, Z. Tonkovic, J. Sorić, and P. Wriggers. A general phase-field model for fatigue failure in brittle and ductile solids. Comp. Mech., 67:1431–1452, 2021.
- 104. F. Xue, T.L. Cheng, Y. Lei, and Y.H. Wen. Phase-field framework with constraints and its applications to ductile fracture in polycrystals and fatigue. npj Comp. Mater., 8, 2022.
- 105. W.D. Reinhardt and R.N. Dubey. Eulerian strain-rate as a rate of logarithmic strain. *Mech. Res. Comm.*, 22(2): 165–170, 1995.
- 106. H. Xiao, O.T. Bruhns, and A. Meyers. Logarithmic strain, logarithmic spin and logarithmic rate. Acta Mech., 124 (1-4):89-105, 1997.
- 107. B. Haghgouyan, C. Hayrettin, T. Baxevanis, I. Karaman, and D.C. Lagoudas. Fracture Toughness of NiTi-Towards Establishing Standard Test Methods for Phase Transforming Materials. Acta Mater., 162:226–238, 2019.
- J.S. Olsen, Z.L. Zhang, H. Lu, and C.V.D. Eijk. Fracture of notched round-bar niti-specimens. Engineering Fracture Mechanics, 84:1–14, 2012.
- J. Makkar and T. Baxevanis. On the fracture response of shape memory alloys by void growth and coalescence. Mechanics of Materials, 153:103682, 2021.
- M. Simoes and E. Martínez-Pañeda. Phase field modelling of fracture and fatigue in shape memory alloys. Comp. Meth. Appl. Mech. Engng., 373:113504, 2021.
- M. Simoes, C. Braithwaite, A. Makaya, and E. Martínez-Pañeda. Modelling fatigue crack growth in shape memory alloys. Fat. Fract. Engng. Mater. Struct., 45:1243–1257, 2022.
- 112. M.E. Gurtin. Generalized Ginzburg-Landau and Cahn-Hilliard equations based on a microforce balance. *Physica D: Nonlin. Phen.*, 92(3):178–192, 1996.
- M. Zhang and T. Baxevanis. An extended three-dimensional finite strain constitutive model for shape memory alloys. J. Appl. Mech., 88(11), 2021.
- 114. D. Lagoudas, D. Hartl, Y. Chemisky, L. Machado, and P. Popov. Constitutive model for the numerical analysis of phase transformation in polycrystalline shape memory alloys. *Int. J. Plast.*, 32:155–183, 2012.
- F. Freddi and G. Royer-Carfagni. Regularized variational theories of fracture: A unified approach. J. Mech. Phys. Solids, 58(8):1154 –1174, 2010.
- L. E. Malvern. Introduction to the Mechanics of a Continuous Medium. Series in Engineering of the Physical Sciences. Prentice-Hall, Inc., Upper Saddle River, NJ, 1969.
- 117. J.C. Simo and T.J.R. Hughes. Computational Inelasticity. Springer-Verlag, Inc., New York, 1998.
- J.Y. Wu and Y. Huang. Comprehensive implementations of phase-field damage models in abaqus. Theor. Appli. Fract. Mech., 106:102440, 2020.
- Y.Navidtehrani, C. Betegón, and E. Martínez-Pañeda. A simple and robust abaqus implementation of the phase field fracture method. Appl. Eng. Sci., 6:100050, 2021.
- 120. T. Wick. Modified newton methods for solving fully monolithic phase-field quasi-static brittle fracture propagation. Comp. Meth. Appl. Mech. Eng., 325:577–611, 2017.
- J.Y. Wu, Y. H., and V. P. Nguyen. On the BFGS monolithic algorithm for the unified phase field damage theory. Comp. Meth. Appl. Mech. Eng., 360:112704, 2020.
- 122. P. K. Kristensen and E. Martínez-Pañeda. Phase field fracture modelling using quasi-newton methods and a new adaptive step scheme. *Theor. Appl. Fract. Mech.*, 107:102446, 2020.
- 123. M. Zhang and T. Baxevanis. Tailoring the anisotropic (positive/zero/negative) thermal expansion in shape memory alloys through phase transformation and martensite (re)orientation. Int. J. Eng. Sc., 177:103687, 2022.
- 124. B. Bourdin, G.A. Francfort, and J.J. Marigo. The variational approach to fracture. J. elast., 91(1):5-148, 2008.
- 125. S. Jape, A. Parrinello, T. Baxevanis, and D.C. Lagoudas. On the Fracture Response of Shape Memory Alloy Actuators. In Ibrahim Karaman, Raymundo Arróyave, and Eyad Masad, editors, TMS Middle East Mediterranean Materials Congress on Energy and Infrastructure Systems (MEMA 2015), page 165, January 2016.